Research Article

# A Molecularly Impermeable Polymer from Two-Dimensional Polyaramids

Cody L. Ritt[1‡], Michelle Quien[1‡], Zitang Wei[1‡], Hagen Gress[2], Mohan T. Dronadula[3], Kaan Altmisdort[2], Yu-Ming Tu[1], Michael Gadaloff[1], Narayana R. Aluru[3], Kamil L. Ekinci[2], J. Scott Bunch*[,2], and Michael S. Strano*[,1]

[1]*Department of Chemical Engineering, Massachusetts Institute of Technology, Cambridge, Massachusetts 02139, USA*
[2]*Department of Mechanical Engineering, Division of Materials Science and Engineering, and the Photonics Center, Boston University, Boston, Massachusetts 02215, USA*
[3]*Oden Institute for Computational Engineering and Sciences, Walker Department of Mechanical Engineering, University of Texas at Austin, Austin, Texas 78712, USA*

*Corresponding authors: Michael Strano, Email: strano@mit.edu, Phone: (617) 324-4323; J. Scott Bunch, Email: bunch@bu.edu, Phone (617) 353-7706
‡These authors contributed equally to this work.

## Abstract/Introductory Paragraph

All polymers exhibit gas permeability through the free volume of entangled polymer chains. However, two-dimensional (2D) materials including graphene stack densely and can exhibit molecular impermeability. Solution-synthesized 2D polymers that exhibit the latter by polycondensation have been a longstanding goal. Herein, we demonstrate self-supporting, spin-coated 2D polyaramid nanofilms that exhibit $N_2$ permeability below $3.1\times10^{-9}$ Barrer, roughly 6500-fold lower than existing polymers, and similar for other gases. Optical interference during the pressurization of nanofilm-coated microwells allows measurement of mechanosensitive rim opening and sealing, creating gas-filled bulges stable exceeding 3 years. This discovery enables 2D polymer resonators with high resonance frequencies (~8 MHz) and *Q* factors up to 537, similar to graphene. A 60-nm coating of air-sensitive perovskites reduces the lattice degradation rate 14-fold with an $O_2$ permeability of $3.3\times10^{-8}$ Barrer. Molecularly impermeable polymers promise the next generation of barrier materials that utilize exceedingly little polymer to maximize chemical rejection, ultimately contributing to sustainable materials development.

## Main Text

Polymeric materials are conventionally thought of as intermediate in order between crystalline and amorphous (*1*). This ordering is described as a two-phase mixture of densely packed crystallite domains dispersed throughout an amorphous phase. The former are considered to be gas-impermeable due to the absence of free volume (*2*). The free volume contribution from the amorphous phase, present even at high crystallinity, gives rise to gas permeability in polymers (*2, 3*). Liquid crystalline polymers, which necessarily assemble as a fluid with minimal free volume, have the lowest reported nitrogen ($N_2$) permeability at ~$10^{-5}$ Barrer (*3, 4*). By contrast, defect-free graphene and its lamellae are ideal crystallites possessing no free volume and, consequently, are impermeable to all gases (*5-7*). While two-dimensional (2D) lattice materials like graphene can exhibit near-perfect gas rejection as nanofilms, they must be grown at high temperatures and manually transferred as macroscopic layers, limiting their use as barrier materials. The processability and formability of conventional polymers allow them to be easily painted, sprayed, and molded onto surfaces, but their residual free volume limits their use as barrier materials. Eliminating free volume with traditional polymers is extremely challenging, if not impossible, as it requires perfect packing of dynamic segmental chains. Polymers that extend covalently in 2D, as we (*8*) and others (*9-11*) have synthesized in the solution phase, can necessarily pack with negligible free volume. Hence, 2D polymers can potentially exhibit barrier properties thus far only observed for 2D inorganic crystalline nanomaterials.

Herein, we use a 2D polyaramid polymer (2DPA-1) synthesized from the polycondensation of melamine and trimesoyl chloride (*8, 12*) to form molecularly impermeable nanofilms between 4–65 nm thick. When dispersed in trifluoracetic acid (TFA) or dimethylsulfoxide (DMSO), 2DPA-1 forms nanoplatelets $\mathcal{O} \sim 10$ nm in diameter (Fig. 1A-B). Unit cells formed by repeating inert amide linkages with triazine cores afford 2DPA-1 a high degree of chemical stability and processability—a consolidation of properties not commonly found in covalent organic framework (COF) analogues (*13*). Powder x-ray diffraction (PXRD) suggests 2DPA-1 lacks long-range order (fig. S1); however, scanning transmission electron microscopy (STEM) of a spin-coated 2DPA-1 thin film reveals layered, orientational ordering (Fig. 1C-E). The latter indicates a center-to-center interlayer spacing of $3.3 \pm 0.2$ Å between stacked 2DPA-1 monolayers. The commensurate ~3.7 Å thickness of monolayer 2DPA-1 platelets (*8*) is consistent with an absence of free volume between 2DPA-1 layers, mirroring multi-layer graphene and molybdenum disulfide (*14*).

To investigate molecular impermeability, nanofilm bulges (*7, 15, 16*) have been used to measure as low as $10^{-11}$ Barrer, or 5 molecules $s^{-1}$ across a 10-$\mu$m diameter microwell at 1 atm. We measured the gas permeation properties of 2DPA-1 films by suspending them over 1-$\mu$m deep microwells, etched into a silicon/silicon oxide ($Si/SiO_2$) wafer with a 285-nm oxide layer. We find that 2DPA-1 nanofilms, even as thin as ~4 nm, are mechanically robust enough to transfer onto the microwell array without rupture (fig. S2), similar to graphene. Also similar, the transfer at room temperature can result in trapped ambient air, producing positively deflected bulges between 50 to 500 nm in height as measured by atomic force microscopy (AFM, Fig. 1F-H and fig. S2). Alternatively, annealing immediately following transfer results in dimpled downward bulges depressed -500 to -190 nm below the well surface (Fig. 1I-K, fig. S3, and Supplementary Text). The deflation rates of the air-trapped bulges lack a thickness dependence, implying that gas leakage is occurring variably through the seal between the 2DPA-1 film and microwell interface.

It is not possible to dynamically observe a well under pressurization using a standard AFM; however, under an optical microscope with an environmental stage, we observe an optical interference effect that allows correlation with physical AFM position by Fourier analysis. Distinct optical profiles arise from changes in the interference of collected light that correspond with the distance between the film and the bottom of the reflective $Si/SiO_2$ microwell, or rather, the deflection (figs. S4-S8). This phenomenon enabled the development of graphene interferometric modulators (*17*) and can be exploited to gain access to real-time deflection monitoring. The effect is strongest for films of 35 nm thickness, and hence, we focus on these below.

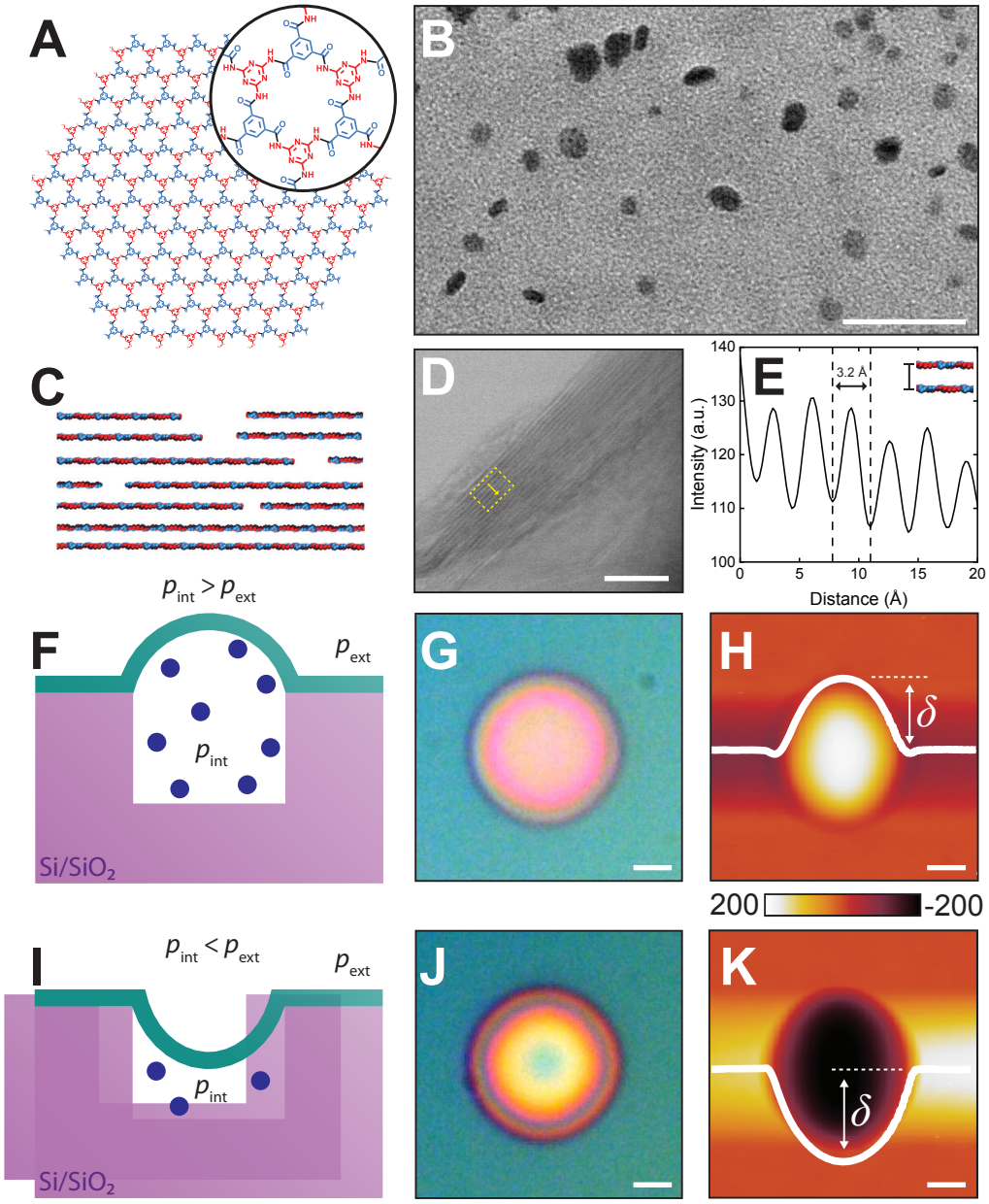


**Fig. 1 | 2DPA-1 Nanoplatelets as Free-Standing Thin Films for Bulge Formation.** (**A**) Theoretical structure of 2DPA-1 nanoplatelets. (**B**) TEM image of TFA-dispersed 2DPA-1 nanoplatelets. Image taken at 110,000× magnification. Scale bar represents 50 nm. (**C**) Theoretical structure of a 2DPA-1 lamella with sparse voids formed due to imperfect packing between neighboring platelets. (**D-E**) Ordering of 2DPA-1 lamella evidenced by STEM (D) and corresponding intensity profile (E). The scale bar represents 5 nm and

the yellow dashed lines indicate the scan region. STEM taken at 4,000,000× magnification. Free-standing 2DPA-1 films, after being transferred onto the $Si/SiO_2$ microwell substrate, forming either (**F-H**) positively deflected bulges or (**I-K**) negatively deflected dimples. (F) and (I) depict cross-sectional illustrations of the film deflections based on the pressure of the internal environment, $p_{int}$, with respect to the external environment, $p_{ext}$. The green layer represents the 2DPA-1 thin film. (G) and (J) are optical micrographs of a bulge and dimple, respectively, with scale bars representing 2 $\mu$m. (H) and (K) are AFM images of the bulge and dimple from (G) and (J), respectively, with scale bars representing 2 $\mu$m and height intensities on the nm-scale. The solid white lines represent cross-sectional deflection profiles taken from AFM, where $\delta$ indicates the overall film deflection.

By utilizing the optical interference described above—and beginning with negatively deflected dimples—we can observe dynamic gas filling using a pressurized microscopy stage (Fig. 2A and fig. S9). The as-formed dimple stipulates that ambient air is unable to enter the microwell and balance the pressure, indicating that, (i), the 2DPA-1 film itself is impermeable to air, and (ii), the seal at the well's rim, formed from van der Waals adhesion between the 2DPA-1 and $SiO_2$ interface, remains intact to prevent leakage. Pressurizing the stage to 150-kPa gauge pressure initially increases the deflection of the film by 6% (from -354 nm to -332 nm) before reversing and depressing to a minimum of -355 nm after almost 1 h. The dimpled film then reverses again, increasing in height before plateauing at roughly -250 nm after 3 h of pressurization. The film does not return to a neutral suspended state (i.e., level with the $SiO_2$ surface) but instead remains depressed within the microwell due to adhesion of the film to the interior of the microwell (fig. S3). The inflection during bulge pressurization corresponds to two competing forces on the bulge – the hydrostatic pressure pushing downward into the well, when the rim is sealed, and inflation from gas filling through the film-substrate interface when the rim is opened. We find that the rim seal can be manipulated in this way using the rate and magnitude of gas pressurization. Further evidence that the pressurized gas, $N_2$ in this case, is sealed within the 2DPA-1-covered well is provided by the formation of stable, positively deflected bulges with deflections that correspond to the applied $N_2$ pressure after releasing to 1 atm (fig. S10).

This direct observation of unsealing and resealing at the microwell rim resolves a longstanding puzzle as to how such 2D material bulges form from pressurization. Previous work postulated that the filling of sealed microwells may be a result of gas diffusion through the $Si/SiO_2$ walls (*7, 16*) due to the relatively close agreement between gas efflux measured from graphene-sealed microwells (*7*) and predictions from classical Fickian diffusion. The observations herein confirm that the substrate-nanofilm adhesion, forming a manipulatable rim seal, provides a greater degree of control over the contents of the resulting bulge. This is the first evidence of a mechano-sensitive opening of the rim seal, further supporting its importance to gating molecular transport from sealed microwells (*6, 18*).

We tracked the deflections for a set of eight bulges from the total 59 that were inflated with 150-kPa $N_2$ for 110 d (Fig. 2B). No statistically significant deflation occurred over that time that would indicate gas escaped the microwell at rates above our measurement detection limit. We confirmed the successful trapping of $N_2$ over that duration by gently puncturing a bulge with an AFM tip, observing it collapse immediately after the pressure was released (fig. S11). The inability of both pressurized $N_2$ to escape bulges and atmospheric $N_2$ to equilibrate negatively pressured dimples, where $\Delta p_{\mathrm{int}} < \Delta p_{\mathrm{atm}}$, points to a film that is $N_2$-impermeable. This finding corroborates

the lack of accessible pore surface area measured for 2DPA-1 platelets via Brunauer–Emmett–Teller (BET), where $N_2$ was used as the probe gas (*8*).

Using the half-life ($t_{1/2}$) of the $N_2$-pressurized bulges that did not deflate over 110 d of observation as a conservative estimate of the bulge lifetime (Supplementary Text), we can threshold the $N_2$ permeability ($P_{N_2}$) of 2DPA-1 below $3.1\times10^{-9}$ Barrer. This permeability, which is nearly four orders of magnitude lower than the least permeable liquid crystalline polymers ($P_{N_2} \approx 2\times10^{-5}$ Barrer), is closer in comparison to the $H_2$ permeability of pristine graphene (Fig. 2B). Furthermore, achieving this level of impermeability necessitates the absence of transmembrane defects, as even the presence of a single 1-nm Knudsen pore would result in $P_{N_2} = 7\times10^{-2}$ Barrer (fig. S12).

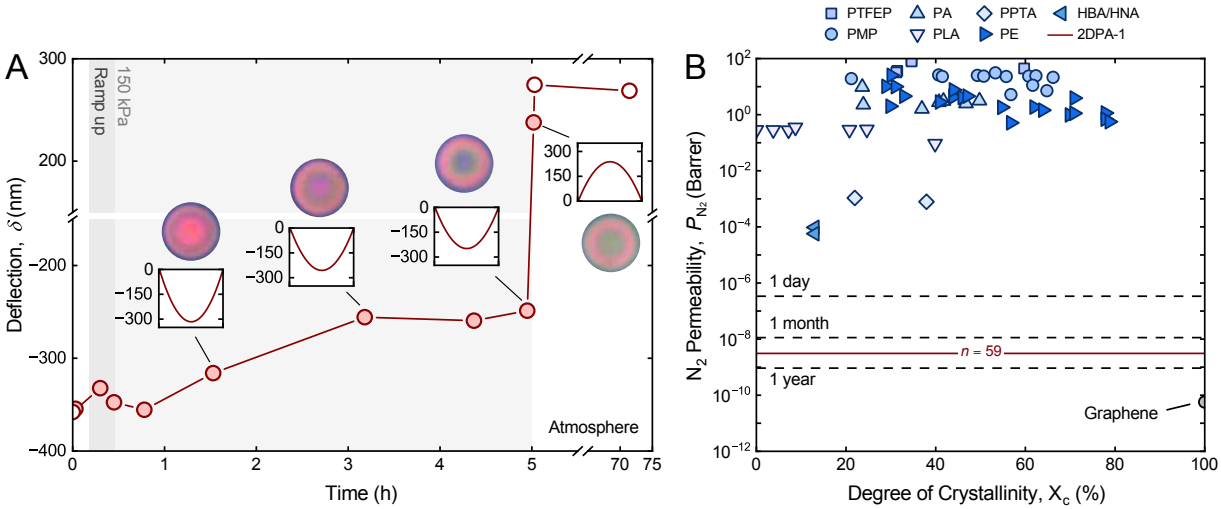


**Fig. 2 | Observation of Dynamic Filling and $N_2$ Impermeability of 2DPA-1.** (**A**) Deflection of 2DPA-1 dimples before, during, and after $N_2$-pressurization in an environmental stage. White- and red-filled datapoints represent deflections determined directly via AFM measurement and indirectly via optical interference analysis, respectively. The dark grey shaded region indicates the pressure ramp-up period from 0 to 150 kPa gauge pressure, whereas the light grey shaded region indicates a 150 kPa gauge pressure of $N_2$. Non-shaded (i.e., white) regions represent atmospheric pressure. The insets show cross-sectional profiles of bulge deflections at respective time steps taken from the optical analyses of the imaged bulges (pictured above insets). (**B**) $N_2$ permeability with respect to degree of crystallinity ($X_c$). The dashed black lines mark the maximum permeability allowed for a 35-nm bulge to remain inflated over various durations for the microwells used in this study. The solid red line represents the threshold permeability for 2DPA-1 based on the observed persistence of 59 2DPA-1-covered microwells over 110 days after filling with 150 kPa $N_2$. The $N_2$ permeability of liquid crystalline and glassy polymers, such as poly[bis(trifluoroethoxy phosphazene)] (PTFEP), polyacrylate (PA), poly(p-phenylene terephthalamide) (PPTA), poly(p-hydroxybenzoic acid-co-6-hydroxy-2-naphthioic acid) (HBA/HNA), poly(4-methyl-1-pentene) (PMP), poly(lactic acid) (PLA), and polyethylene (PE) are included for comparison, along with the $H_2$ permeability of graphene.

The impermeability of 2DPA-1 implies an absence of free volume required for molecular transport. The pore within the 2DPA-1 unit cell is estimated to be approximately 1 nm in diameter; hence, it is unlikely that a monolayer platelet would impose substantial resistance to most gas molecules (*19*). We suspect the impermeability necessitates a staggered configuration of stacked

2DPA-1 bilayers, similar to AB stacking in COFs (*20, 21*), to reduce the effective pore size, enhance chemical interactions, and eliminate free volume. Assuming complete steric exclusion, a pore-to-pore offset of 61% imposes the greatest steric restriction to molecular transport. Hit-and-miss Monte Carlo simulations (*22-24*) that assume hard-sphere interactions to estimate molecular accessibility are in good agreement (figs. S13-S14), arriving at an offset of 65%. Notably, Monte Carlo simulations show that $N_2$ permeation can be sterically eliminated when the center-to-center pore offset is between 65–80%. Using high-throughput density functional theory (DFT) and molecular dynamics (MD) simulations as more accurate proxies for molecular accessibility (figs. S15-S19), we calculated the $N_2$ translocation energy barrier across a bilayer pore to be 65.6 kJ $mol^{-1}$ in the most occluded scenario. The total energy barrier increases to 77.0 kJ $mol^{-1}$ when accounting for sequential hopping throughout a 100-layer (~35-nm) film and lays between values measured for extremely thick ($\sigma \sim \mu$m) crystalline polymers (*25, 26*) and pristine monolayer graphene (*5*).

The ability of 2DPA-1 films to trap gas within the microwells is not exclusive to $N_2$. We observed similar multi-day persistence for bulges filled with sulfur hexafluoride ($SF_6$), argon (Ar), and methane ($CH_4$, Fig. 3A-D), suggesting that 2DPA-1 is likewise impermeable to gases larger or similar in size to $N_2$. We note that the formation of persistent bulges was not observed for smaller gases such as oxygen ($O_2$), carbon dioxide ($CO_2$), helium (He), or hydrogen ($H_2$, table S1). The mechanistic reasoning for this observation is not straightforward. The inability to form persistent bulges when filling with these smaller gases could invoke a size exclusion mechanism; however, as evidenced with $N_2$ filling, the persistence of a bulge is strongly coupled to the interfacial rim seal for each microwell. It is not yet known how different gases may interact with or alter the rim seal, thereby convoluting our interpretation of the exact escape mechanism. For the gases that generated persistent bulges, it is evident that gas transport only occurs during the pressurization process when the rim seal opens.

The fluctuations in the bulge deflections over time appear to vary randomly from day to day by ~5% on average (fig. S20). This behavior is similar to previous observations of leak-free graphene bulges (*6, 27*) and resembles a random walk. We analyzed these random fluctuations by comparing the mean square displacement (MSD) of the bulge deflection with respect to time (Figure 3E-H and figs. S21-22). Data from leak-free graphene bulges (*6*) follow a confined diffusion, where the MSD plateaus at a limiting value. The MSD of 24 air-trapped 2DPA-1 bulges measured over 1000 d similarly plateaued, reaching a limiting value around 200 d. Notably, the squared confinement length taken from this analysis correlates strongly ($R^2 = 0.92$) with the initial deflection of the bulges (Figure 3I). Given the inherent relationship between the bulge deflection and internal pressure, MSD analysis may present itself as a new, practical tool for estimating the pressure of sealed microwell systems where the internal pressure is unknown. Further, the longitudinal robustness of the inflated bulges indicates 2DPA-1 does not become permeable over time due to hygroscopic degradation common to 1D polyaramids (e.g., Kevlar) or physical aging phenomena ubiquitous to polymer systems (*28*), often manifesting in the form of altered free volume due to the relaxation of polymer chains (*29*). 2D polyaramids thus represent an entirely new and exciting class of barrier materials—possessing the low permeability properties of 2D crystals in tandem with the synthetic processability of traditional polymers.

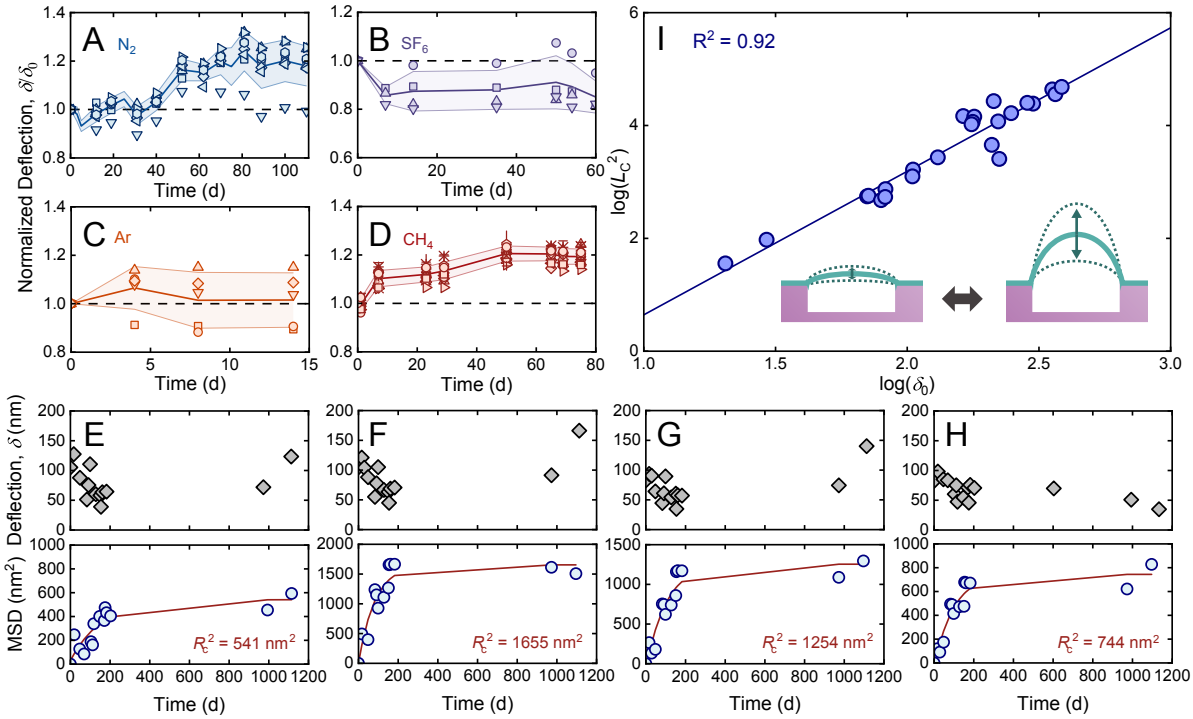


**Fig. 3 | Confined Diffusion of Gases Sealed Within Microwell.** (**A-D**) Normalized deflection of bulges filled with (A) $N_2$, (B) $SF_6$, (C) Ar, and (D) $CH_4$ measured over time. The solid, colored lines and shaded regions represent the average and standard deviation of the bulge measurements at each time point, respectively. The dashed black line marks the initial deflection, $\delta_0$, for all bulges. (**E-H**) Mean square displacement, MSD, analysis for four 2DPA-1 bulge deflections measured over 1000 d. Bulge deflections are represented as grey diamonds (top). The MSD of these deflection data, represented as light blue circles (bottom), are fit to a squared confinement length, $R_C^2$, via eq. S14 for confined diffusion (red line). (**I**) Logarithm of $\delta_0$ with respect to the logarithm of $R_C^2$. Datapoints are taken from (E-H) and fig. S22. The solid curve represents a linear regression between the two variables with $R^2 = 0.92$. The inset illustrates the increase in $R_C^2$, depicted as variation in the bulge deflection, for systems with greater initial deflections.

Our exciting findings warrant the question, what characteristics of 2DPA-1 platelets give rise to impermeable films? Platelet size can have a prodigious effect on the gas permeability of a film, as higher aspect ratio platelets are more likely to lead to environments with reduced free volume (*30*). We estimate the size of dispersed 2DPA-1 platelets using nuclear magnetic resonance (NMR) end-group analysis as it is compatible with both TFA and DMSO dispersion solvents. The aromatic- and end group-protons on 2DPA-1 are detectable in NMR, and the ratio of peak integrations between the two is the aromatic end group ratio ($r$) that can be used to estimate the platelet size (figs. S23-S25, Methods). At longer reaction times, $r$ increases monotonically and agrees well with theoretical values calculated for perfect hexagonal polycyclic structures. Analyzing aromatic peaks from $^1$H NMR spectra of 2DPA-1 reveals a downshift in the aromatic peak positions with respect to reaction time. As 2DPA-1 platelets get larger, more electron-withdrawing carbonyl groups are introduced into the polymer matrix, consequently deshielding aromatic protons (*31*). We introduce the concept of skewness ($s$) to further analyze aromatic peak

shifting, calculated as the normalized difference between the mean and mode of the aromatic peak distribution. The *s* parameter provides an orthogonal measure of polycyclic aramid growth (*32*).

By combining both *r* and *s* parameters in a two-dimensional trajectory, we can clearly differentiate polycyclic aramids from dendrimers (Fig. 4A). We see that experimental datapoints for *r* and *s* parameters converge toward a theoretical threshold with increasing reaction time. By contrast, the dendrimers exhibit positive *s* values and they are bounded by an upper limit of 2 for the *r* parameter. The *r* parameter proves invaluable in estimating the theoretical platelet size of 2DPA-1 and gauging the relative defectiveness of the platelets (Fig. 4B-C, figs. S26-S27). Nanoplatelet size scales linearly with respect to the *r* parameter, whereas dendrimer size holds no practical relationship with *r*. This scaling is confirmed by TEM and solution-phase fluorescence measurements, and it is found to be critical to forming mechanically robust 2DPA-1 films that can suspend over the microwells (figs. S27-29, Supplementary Text).

Nanoelectromechanical devices ranging from nanoscale resonators to molecular valves have implications for information processing, molecular manipulation, and sensing applications (*33*). The vibration of nanoscale resonators in response to an applied external force improves as the resonant frequency increases and the resonator mass decreases (*34*), making ultrathin films ideal candidates. We measured the thermal fluctuation of a 35-nm 2DPA-1 bulge optically under vacuum ($\sim 10^{-7}$ Torr) and detected a resonant frequency in the megahertz range (Fig. 4I and fig. S30). The initial deflection was measured by AFM. Prolonged vacuum exposure led to total bulge deflation, determined by interferometry, and coincided with an increase in the quality factor ($Q$) from 87 to 537. $Q$ describes the efficiency of the resonator in terms of energy loss. While energy losses associated with changes in adhesion at the inner wall of the microwell can affect the measured $Q$, the six-fold increase in $Q$ is likely due to decreased damping as gas molecules evacuate the microwell (*34*). This finding further validates the successful trapping of $N_2$ within the 2DPA-1-sealed microwell and represents, to our knowledge, the first-ever polymer resonator approaching molecular thinness (i.e., sub-10 nm)—presenting myriad opportunities for new scientific exploration.

The facile processability of a mechanically robust and transmembrane defect-free film is crucial to the practical scaling and implementation of 2DPA-1 as a molecular barrier. To demonstrate the potential for scale up, we directly spin coated methylammonium lead iodide ($MAPbI_3$) 3D perovskite thin films (1 cm × 1 cm) with 60 nm of 2DPA-1 to encapsulate the perovskite and assess inhibition of $O_2$ and water vapor by 2DPA-1 (Fig. 4F-H). $MAPbI_3$ is extremely sensitive to $O_2$ and water (*35*), completely degrading to lead iodide ($PbI_2$) after only 3 d of air exposure. Conventional encapsulation methods for 3D perovskites, such as UV-curable adhesives and single-layer hydrophobic encapsulation, typically require coatings over 100 $\mu$m thick (*36*). By contrast, encapsulating the perovskite with only a 60-nm-thick protection layer of 2DPA-1 markedly retards the degradation of $MAPbI_3$—extending its stability to 21 d under ambient conditions, with negligible degradation observed over the first 7 d. We monitored the degradation kinetics of the 2DPA-1-coated and uncoated systems by comparing the relative intensities of the $MAPbI_3$ (110) and $PbI_2$ (001) XRD peaks over time (fig. S31, Methods). The retarded degradation kinetics of the 2DPA-1-coated perovskite begets an estimated $O_2$ permeability of $3.3\times10^{-8}$ Barrer. This value is several orders of magnitude lower than existing crystalline polymers and implies that the lack of persistent bulge formation upon $O_2$ pressurization is a result of inadequate sealing of the microwell interface, potentially induced by interactions

between $O_2$ and 2DPA-1 chemical groups. More importantly, this demonstrates the capability of 2DPA-1 to be scaled to larger dimensions than the $\mu$m-scale of the $Si/SiO_2$ wells without failing from defect formation, such as cracks or pinholes that commonly plague thin films made of inorganic 2D materials (*24, 37*).

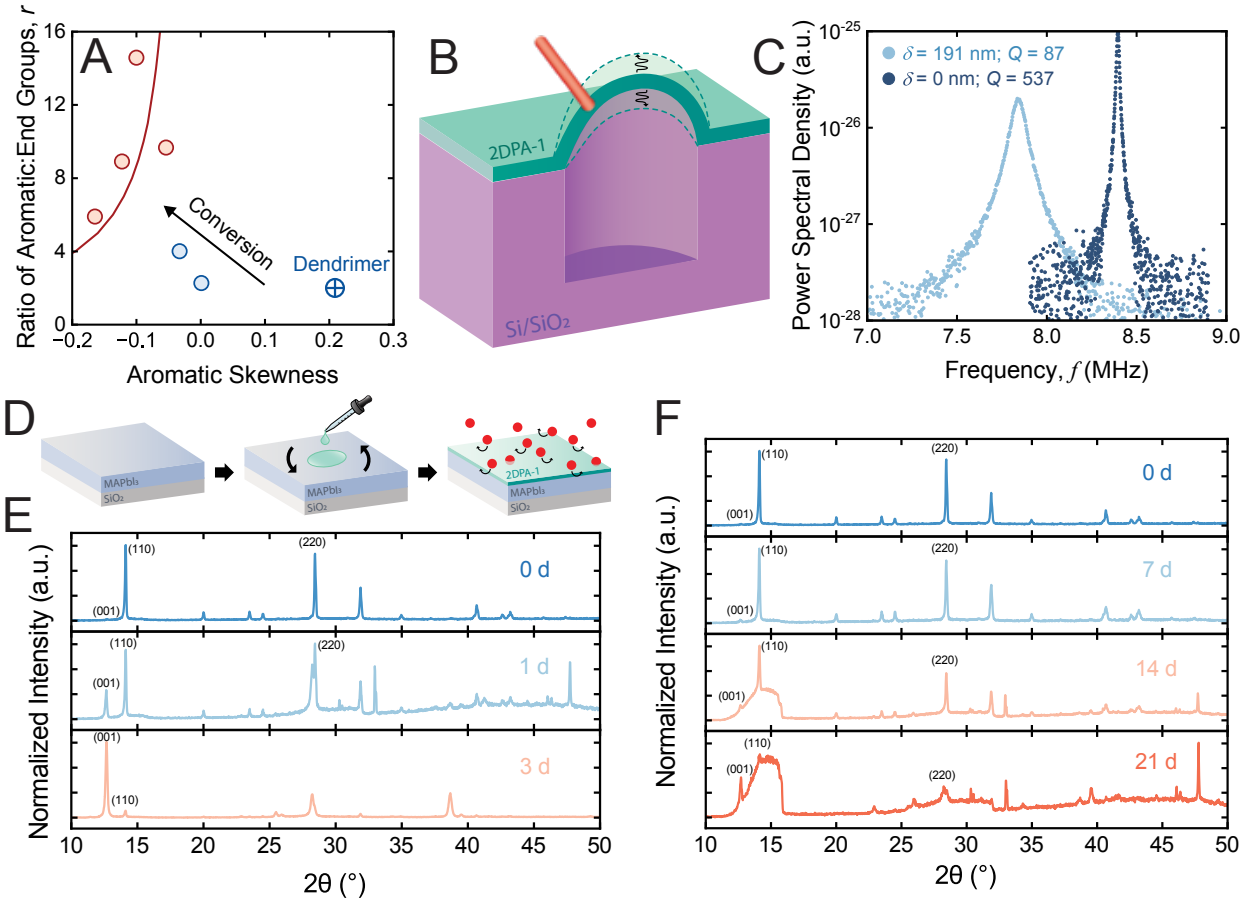


**Fig. 4 | Scaling 2DPA-1 for Practical Applications.** (**A**) Theoretical and experimental aromatic-to-end group ratio, *r*, versus aromatic skewness, *s*. Shown are the dendritic limit (blue circle with cross), the polycyclic curve for $r > 4$ (solid red line), and experimental (*r*, *s*) points for reaction aliquots extracted at various times during synthesis that trace a trajectory towards and then along the polycyclic curve from the dendritic limit. Solid red datapoints indicate perfect polycyclic 2DPA-1 platelets that can form mechanically stable, suspended thin films. Solid blue datapoints are 2DPA-1 platelets intermediate between polycyclic and dendritic that cannot form suspended films. (**B**) Illustration of a suspended 2DPA-1 film as a nanoelectromechanical resonator, where the thermal vibrations of the film are detected by a focused diode laser. (**C**) Power spectral density versus frequency, *f*, for the fundamental mode of a 35-nm-thick 2DPA-1 resonator under $10^{-7}$ Torr vacuum. Dark blue data are taken after initial introduction to vacuum, whereas light blue data is the final measurement after complete gas evacuation from the microwell. (**D**) Illustration of 2DPA-1 spin-coating process on $MAPbI_3$ 3D perovskite to assess its inhibition of $O_2$ and $H_2O$ (red circles) permeation. (**E-F**) XRD spectra of $MAPbI_3$ films that were (E) uncoated and (F) coated with at 60-nm 2DPA-1 film. Stacked panels show the change in spectra with respect to time exposed to ambient air. The (110) and (220) peaks represent signature peaks of $MAPbI_3$. The (001) peak represents the signature peak of the degradation byproduct, $PbI_2$. Insets are optical images of the perovskite films over time.

## Acknowledgements

This work was primarily supported as part of the Center for Enhanced Nanofluidic Transport–Phase 2 (CENT$^2$), an Energy frontier Research Center funded by the U.S. Department of Energy, Office of Science, Basic Energy Sciences under Award #DE-SC0019112. K.A. was supported by funding from the Distinguished Summer Research Fellowship (DSRF) and the Undergraduate Research Opportunities Program (UROP) at Boston University. The authors acknowledge the use of the parallel computing resource Lonestar6 provided by the Texas Advanced Computing Center (TACC) at The University of Texas at Austin. Synthetic work was carried out in part under auspices of the Institute for Soldier Nanotechnologies (ISN), whereas material characterization was carried out in part through the use of MIT.nano's facilities. We thank Junze Qin and Samuel Eppley for their assistance with deflection measurements for gas-pressurized bulges, as well as David Lloyd and Sungyun Yang for their help fabricating and preparing the etched substrates used for gas permeation measurements.

## Data availability statement

All data needed to support the conclusions of this manuscript are included in the manuscript or supplementary materials.

## Conflict of interest

The authors have no conflict of interest to declare.

## Supplementary Materials

Materials and Methods
Supplementary Text
Figs. S1 to S31
Tables S1 to S2
References

## References


1. S. Kavesh, J. Schultz, Meaning and measurement of crystallinity in polymers: A review. *Polym. Eng. Sci.* **9**, 331-338 (1969).
2. B. D. Freeman, A. J. Hill, Free Volume and Transport Properties of Barrier and Membrane Polymers in *Structure and properties of glassy polymers*. (American Chemical Society, 1999), vol. 710, chap. 21, pp. 306-325.
3. S. Kanehashi, A. Kusakabe, S. Sato, K. Nagai, Analysis of permeability; solubility and diffusivity of carbon dioxide; oxygen; and nitrogen in crystalline and liquid crystalline polymers. *J. Membr. Sci.* **365**, 40-51 (2010).
4. A. W. Thornton, B. D. Freeman, L. M. Robeson, Polymer gas separation membrane database (2012) https://membrane-australasia.org/polymer-gas-separation-membrane-database/.
5. L. Tsetseris, S. T. Pantelides, Graphene: An impermeable or selectively permeable membrane for atomic species? *Carbon* **67**, 58-63 (2014).
6. P. Z. Sun *et al.*, Limits on gas impermeability of graphene. *Nature* **579**, 229-232 (2020).
7. J. S. Bunch *et al.*, Impermeable atomic membranes from graphene sheets. *Nano Lett.* **8**, 2458-2462 (2008).
8. Y. W. Zeng *et al.*, Irreversible synthesis of an ultrastrong two-dimensional polymeric material. *Nature* **602**, 91-95 (2022).
9. K. Baek *et al.*, Free-standing, single-monomer-thick two-dimensional polymers through covalent self-assembly in solution. *J. Am. Chem. Soc.* **135**, 6523-6528 (2013).
10. N. Hosono, S. Mochizuki, Y. Hayashi, T. Uemura, Unimolecularly thick monosheets of vinyl polymers fabricated in metal–organic frameworks. *Nat. Comm.* **11**, 3573 (2020).
11. K.-D. Zhang *et al.*, Toward a single-layer two-dimensional honeycomb supramolecular organic framework in water. *J. Am. Chem. Soc.* **135**, 17913-17918 (2013).
12. G. Zhang, Y. Zeng, P. Gordiichuk, M. S. Strano, Chemical kinetic mechanisms and scaling of two-dimensional polymers via irreversible solution-phase reactions. *J. Chem. Phys.* **154**, 194901 (2021).
13. X. Li *et al.*, Chemically robust covalent organic frameworks: Progress and perspective. *Matter* **3**, 1507-1540 (2020).
14. A. Keerthi *et al.*, Ballistic molecular transport through two-dimensional channels. *Nature* **558**, 420-424 (2018).
15. L. Wang *et al.*, Molecular valves for controlling gas phase transport made from discrete ångström-sized pores in graphene. *Nat. Nanotechnol.* **10**, 785-790 (2015).
16. S. P. Koenig, L. D. Wang, J. Pellegrino, J. S. Bunch, Selective molecular sieving through porous graphene. *Nat. Nanotechnol.* **7**, 728-732 (2012).
17. S. J. Cartamil-Bueno *et al.*, Graphene mechanical pixels for interferometric modulator displays. *Nat. Comm.* **9**, 4837 (2018).
18. Y. Manzanares-Negro *et al.*, Improved graphene blisters by ultrahigh pressure sealing. *ACS Appl. Mater. Interfaces* **12**, 37750-37756 (2020).
19. H. Fan *et al.*, High-flux vertically aligned 2D covalent organic framework membrane with enhanced hydrogen separation. *J. Am. Chem. Soc.* **142**, 6872-6877 (2020).
20. P. H. H. Duong *et al.*, Molecular interactions and layer stacking dictate covalent organic framework effective pore size. *ACS Appl. Mater. Interfaces* **13**, 42164-42175 (2021).

21. X. Wu, X. Han, Y. Liu, Y. Liu, Y. Cui, Control interlayer stacking and chemical stability of two-dimensional covalent organic frameworks via steric tuning. *J. Am. Chem. Soc.* **140**, 16124-16133 (2018).
22. C. Sun *et al.*, Mechanisms of molecular permeation through nanoporous graphene membranes. *Langmuir* **30**, 675-682 (2014).
23. Z. Yuan *et al.*, Gas separations using nanoporous atomically thin membranes: Recent theoretical, simulation, and experimental advances. *Adv. Mater.* **34**, 2201472 (2022).
24. C. L. Ritt, J. R. Werber, A. Deshmukh, M. Elimelech, Monte carlo simulations of framework defects in layered two dimensional nanomaterial desalination membranes: Implications for permeability and selectivity. *Environ. Sci. Technol.* **53**, 6214-6224 (2019).
25. S. Allen, M. Fujii, V. Stannett, H. Hopfenberg, J. Williams, The barrier properties of polyacrylonitrile. *J. Membr. Sci.* **2**, 153-163 (1977).
26. J. Chiou, D. Paul, Gas transport in a thermotropic liquid-crystalline polyester. *J. Polym. Sci., Part B: Polym. Phys.* **25**, 1699-1707 (1987).
27. Z. Wu *et al.*, Proton and molecular permeation through the basal plane of monolayer graphene oxide. *Nat. Comm.* **14**, 7756 (2023).
28. J. M. Hutchinson, Physical aging of polymers. *Prog. Polym. Sci.* **20**, 703-760 (1995).
29. H. W. H. Lai *et al.*, Hydrocarbon ladder polymers with ultrahigh permselectivity for membrane gas separations. *Science* **375**, 1390-1392 (2022).
30. M. A. Osman, A. Atallah, High-density polyethylene micro-and nanocomposites: Effect of particle shape, size and surface treatment on polymer crystallinity and gas permeability. *Macromol. Rapid Commun.* **25**, 1540-1544 (2004).
31. G. Gribble, F. Bousquet, Deshielding effects in the NMR spectra of ortho-substituted anilides and thioanilides. *Tetrahedron* **27**, 3785-3794 (1971).
32. Z. Wei, Y.-M. Tu, W. Yim, M. Quien, A.A. Alizadehmojarad, X. Gong, M.S. Strano, $^{1}$H NMR trajectories for analyzing the growth and purification of 2D polyaramids. *J. Am. Chem. Soc.* (under review).
33. J. S. Bunch *et al.*, Electromechanical resonators from graphene sheets. *Science* **315**, 490-493 (2007).
34. K. Ekinci, M. Roukes, Nanoelectromechanical systems. *Rev. Sci. Instrum.* **76**, (2005).
35. J. Hidalgo *et al.*, Synergistic role of water and oxygen leads to degradation in formamidinium-based halide perovskites. *J. Am. Chem. Soc.* **145**, 24549-24557 (2023).
36. S. Ma *et al.*, Development of encapsulation strategies towards the commercialization of perovskite solar cells. *Energy Environ. Sci.* **15**, 13-55 (2022).
37. M. S. Boutilier *et al.*, Implications of permeation through intrinsic defects in graphene on the design of defect-tolerant membranes for gas separation. *ACS Nano* **8**, 841-849 (2014).